

ORIGINAL ARTICLE

Beam switching and bifocal zoom lensing using active plasmonic metasurfaces

Xinghui Yin^{1,2}, Tobias Steinle¹, Lingling Huang³, Thomas Taubner⁴, Matthias Wuttig⁴, Thomas Zentgraf⁵ and Harald Giessen¹

Compact nanophotonic elements exhibiting adaptable properties are essential components for the miniaturization of powerful optical technologies such as adaptive optics and spatial light modulators. While the larger counterparts typically rely on mechanical actuation, this can be undesirable in some cases on a microscopic scale due to inherent space restrictions. Here, we present a novel design concept for highly integrated active optical components that employs a combination of resonant plasmonic metasurfaces and the phase-change material Ge₃Sb₂Te₆. In particular, we demonstrate beam switching and bifocal lensing, thus, paving the way for a plethora of active optical elements employing plasmonic metasurfaces, which follow the same design principles.

Light: Science & Applications (2017) 6, e17016; doi:10.1038/lsa.2017.16; published online 28 July 2017

Keywords: active; beam-forming; metasurfaces; phase-change material; plasmonics

INTRODUCTION

Form follows function¹—this principle heeded by generations of modernist architects is not only a guideline, but rather the unyielding maxim dictated by Snell's law of refraction² when it comes to lens design³. The curvatures of material interfaces used to craft wave fronts closely follow from the intended function the optical element is to perform. Active optical elements, then, naturally carry out their task by reshaping themselves according to the changing requirements they have to fulfill in different situations. The lens of the human eye, for example, increases its curvature when adapting from looking at a distant object to one close by. Similarly, deformable mirrors used in astronomy reconfigure their surface to compensate for wave front distortions stemming from atmospheric disturbances. However, with the advent of metasurfaces—artificial subwavelength thickness materials—and moreover the formulation of a generalized Snell's law^{4,5}, form has detached from function. A metasurface lens^{6–12} can be completely flat, yet impart a spatially varying phase profile through abrupt phase jumps and thus shape the wave front of a transmitted light wave. Therefore, optical elements utilizing active metasurfaces can accomplish varying functions exploring entirely different approaches that are geometrically static, which is a key advantage of metasurface based optical components^{13,14}.

A field closely linked to metasurfaces is plasmonics, the study of light interaction with free electrons in a metal, which has already realized active designs that do not rely on mechanical deformation. Moreover, graphene^{15–18}, injection of free carriers in semiconductors^{19–23}, phase transition materials such as VO₂^{24–26},

gallium^{27,28}, yttrium-hydride²⁹ magnesium³⁰, and the phase-change material GeSbTe (GST)^{31–34} have been successfully employed to achieve active plasmonics. In particular, GST has also been used on its own to demonstrate reconfigurable amplitude masks for compact optical components³⁵ that retain their functionality without external stimuli. This is possible due to the fact that phase-change materials possess phases that are metastable at room temperature.

MATERIALS AND METHODS

Metasurface fabrication

Beam-switching and bifocal lensing concepts are demonstrated using metasurface nanostructures that are fabricated on top of a 50 nm GST-326 film that was DC-magnetron sputter-deposited with a background pressure of 2×10^{-6} mbar and 20 sccm Ar flow followed by sputtering of a 15 nm protective layer of ZnS:SiO₂.

Subsequently, the gold nanostructure metasurface was prepared using electron beam lithography employing a polymethylmethacrylate (PMMA) double layer resist, where the first layer is 100 nm 3.5% 200K PMMA and the second layer 100 nm 1.5% 950K PMMA. The resist was baked for 2 min at 120 °C after each layer. After development in 3:1 MIBK:isopropyl alcohol, 2 nm of chromium followed by 40 nm of gold were thermally evaporated and a lift-off was carried out.

Simulation

The simulations were carried out using finite-difference time-domain Solutions by Lumerical Inc. with periodic boundary conditions and perfectly matched layers for the beam switching and bifocal lens

¹4th Physics Institute and Research Center SCoPE, University of Stuttgart, 70550 Stuttgart, Germany; ²Max-Planck-Institute for Solid State Research, Heisenbergstrasse 1, 70569 Stuttgart, Germany; ³Beijing Institute of Technology, No. 5 South Zhongguancun Street, Beijing 100081, China; ⁴I. Institute of Physics (IA), RWTH Aachen University, 52056 Aachen, Germany and ⁵Department of Physics, University of Paderborn, Warburger Straße 100, 33098 Paderborn, Germany
Correspondence: X Yin, Email: x.yin@pi4.uni-stuttgart.de

Received 13 September 2016; revised 13 February 2017; accepted 14 February 2017; accepted article preview online 6 June 2017

metasurfaces respectively. The metasurface was placed on a CaF₂ substrate with 1.47 refractive index followed by either 50 nm of a- or c-GST respectively (refractive index data from Ref. 32) and 15 nm of ZnS:SiO₂ with refractive index 2. We used RCP plane wave excitation centered at 3.1 μm and evaluated the field intensity of LCP light behind the metasurface.

Experimental setup for measuring beam switching concept metasurface

The optical properties of the beam steering metasurface were measured using a home-built master-oscillator-parametric-amplifier (MOPA)³⁶ operating at 1033 nm pump wavelength and 3100 nm idler wavelength, which was used to characterize the active metasurface. The collimated beam is linearly polarized and was passed through a quarter waveplate before passing through the metasurface and impinging on a pyroelectric array camera (Pyrocam III, Ophir Photonics) (*cf.* Supplementary Fig. S1).

Experimental setup for measuring bifocal lens concept metasurface

We used the same home-built MOPA light source set to 3100 nm to characterize the varifocal lens. A quarter waveplate was introduced to the beam path before the metasurface to generate right-handed circularly polarized light. After passing through the sample, the light was collected with a 20× objective and sent through a second quarter waveplate and linear polarizer set to transmit only left-handed circularly polarized light. Subsequently, the resulting two-dimensional (2D) intensity distribution was imaged on a pyroelectric camera (Pyrocam III, Ophir Photonics). The sample was mounted on a linear translation stage with a micrometer screw gauge, allowing for the imaging of different *z*-planes every 100 μm. (*cf.* Supplementary Fig. S2).

RESULTS AND DISCUSSION

Here, we present a novel approach for the design of active plasmonic nanophotonic components that combines metasurfaces with the low-loss phase-change material (PCM) Ge₃Sb₂Te₆ (GST-326)^{32,37}. In particular, we make use of the large contrast of the optical dielectric constants between the amorphous ($n_a \approx 3.5 + 0.001i$) and crystalline phases ($n_c \approx 6.5 + 0.06i$) at *ca.* 3.1 μm (*cf.* Supplementary Fig. S4). In our proof-of-concept demonstration, two different sets of plasmonic antenna elements A and B provide distinct functionalities, for example, beam refraction to opposite directions, but are spatially staggered within one light interaction area on top of a GST layer (Figure 1a). Depending on the state of the phase-change material, one can select which set of plasmonic antennas strongly interacts with the incident light at a certain operating wavelength. This is achieved by choosing appropriate lengths for A and B type antennas such that their respective plasmon resonance wavelengths match the operating wavelength either in the amorphous or crystalline PCM state (Figure 1b). Therefore, switching the PCM selectively 'activates' a subset of metasurface elements, which is reminiscent of early work on frequency selective surfaces^{38,39}. The concept of staggering different designs into one layout crucially hinges on the inherent local surface plasmon resonance property of exhibiting extinction cross-sections at resonance that are much larger than the geometrical footprints of the individual antenna elements. This allows for elements to be spaced relatively far apart from one another while retaining an effectively continuously covered surface from a light interaction view point. The only limiting factor in designing staggered metasurfaces lies in avoiding propagating surface modes such as Rayleigh anomalies stemming from a periodic arrangement of plasmonic antenna

elements with certain periodicities that might introduce undesired loss channels.

First, we demonstrate the principle for constructing bi-functional active plasmonic devices employing a plasmonic beam-switching metasurface that refracts an incident beam in opposite directions depending on the phase of the active PCM layer. We utilize a dispersionless geometric phase approach⁴⁰ to design abrupt phase jumps Φ at the metasurface where the relative rotation angle of a nanorod antenna is directly related to the phase that is picked up by the cross-converted fraction of incident circularly polarized light (CPL). The cross-converted field scattered by the antennas arises from the dipole moment \mathbf{p} that is induced by an incident electric field, which impinges on a dipole that forms an angle φ with the *x* axis in the *x*-*y* plane as follows:

$$\mathbf{p}_{L(R)} = (a_1 \mathbf{e}_{L(R)} \pm a_2 e^{\pm i2\varphi} \mathbf{e}_{R(L)}),$$

where a_1, a_2 are the co- and cross-polarization amplitudes, respectively, the subscripts R and L denote right- and left-handed circularly polarized light, respectively, and $\mathbf{e}_{L(R)}$ are the unit vectors for left- and right-handed circularly polarized light. The sign in the exponent depends on the combination incidence/transmission and is positive for LCP/RCP and negative for RCP/LCP. Thus, a continuously full 0 to 2π range of abrupt phase jumps $\Phi = 2\varphi$ can be realized by rotating the electric dipole, that is, a plasmonic nanorod antenna, in the *x*-*y* plane from 0 to π ⁴⁰. Therefore, arranging *m* nanorods equally spaced over a superperiod Λ with relative rotation angles of π/m in between adjacent elements yields a constant phase gradient $d\Phi/dx$. The generalized Snell's law for the converted circularly polarized light is then⁴

$$n_t \sin \theta_t - n_i \sin \theta_i = \frac{\lambda_0 d\Phi}{2\pi dx} = \pm \frac{\lambda_0 d\varphi}{\pi dx} = \pm \frac{\lambda_0}{\Lambda}$$

Using this principle, we construct the unit cell of the beam-switching active plasmonic metasurface to consist of two rows of $m=15$ antennas A and B with lengths $l_A=600$ nm and $l_B=370$ nm, thicknesses $t_A=t_B=40$ nm and widths $w_A=w_B=50$ nm. The antennas are made of gold and are equally spaced in *x*-direction with periodicity $p=900$ nm, and distance between rows A and B as $d=550$ nm (Figure 2a). This results in plasmon resonances at $\lambda_0=3.2$ μm for antennas A on an a-GST layer and antennas B on a c-GST layer. The superperiod Λ is 13.5 μm, which yields a refraction angle of $\theta_{t=}$ $\pm 13.28^\circ$, depending on the helicity of the incident light. The nanorods in the upper row are rotated clockwise going from left to right whereas those in the lower row are rotated anti-clockwise leading to opposite refraction angles for the same helicity of incident circularly polarized light. Full-field finite-difference time-domain simulations were carried out for the unit cell with periodic boundary conditions in *x*- and *y*-directions. The metasurface is located at $z=0$ and illuminated from the top at normal incidence with RCP light. The resulting phase profile of a cut through the *x*-*z* plane demonstrates the refraction to opposite angles for cross-converted light (LCP) a-GST and c-GST (Figure 2b). The normalized transmittance spectra reveal that antennas A are resonant around 3.2 μm in the a-GST case, whereas antennas B's resonance shifts to this spectral position in the c-GST case. Note, that the transmittance values above a value of 1 are due to the excitation of grating modes, which leads to more light being funneled through the same interaction area with respect to the background area used for normalization. The state of the phase-change material thus selects whether antenna set A or B interacts with the incident light, which fundamentally differs from previous approaches where the incident state of light selected, which part of the metasurface would be interacting⁴¹⁻⁴³.

We fabricated the design using electron beam lithography over an area of $600\ \mu\text{m} \times 600\ \mu\text{m}$ to define the plasmonic gold nanorods. As substrate, we used CaF_2 with a 50 nm thick layer of GST-326 followed

by a 15 nm thick ZnS:SiO_2 capping layer to prevent oxidation and chemical isolation between the GST and gold. A scanning electron micrograph of the resulting metasurface is shown in Figure 3a. In

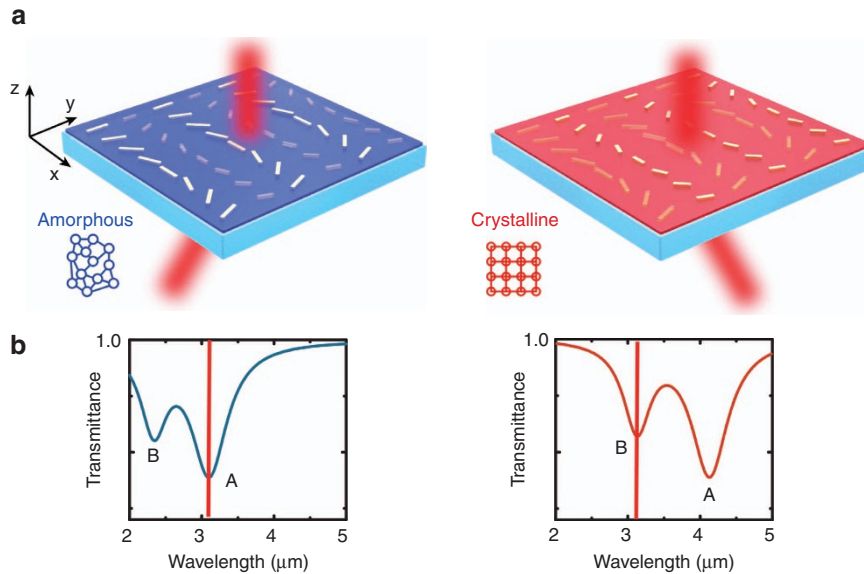


Figure 1 Active plasmonic metasurface for beam switching. The active metasurface consists of a 50 nm thick GST-326 layer underneath a geometric phase metasurface for beam switching. Two types of nano-antennas A and B with different plasmon resonances are alternated line-wisely. (a) When the active layer is in the amorphous phase, only type A rods interact with the incident light at $3.1\ \mu\text{m}$ wavelength and deviate the beam (left). When the active layer is in the crystalline phase, only type B rods interact with the incident light and deviate the beam into the opposite direction due to their relative orientation (right). (b) Schematic depiction of transmittance of active metasurface in the amorphous (left) and crystalline (right) state.

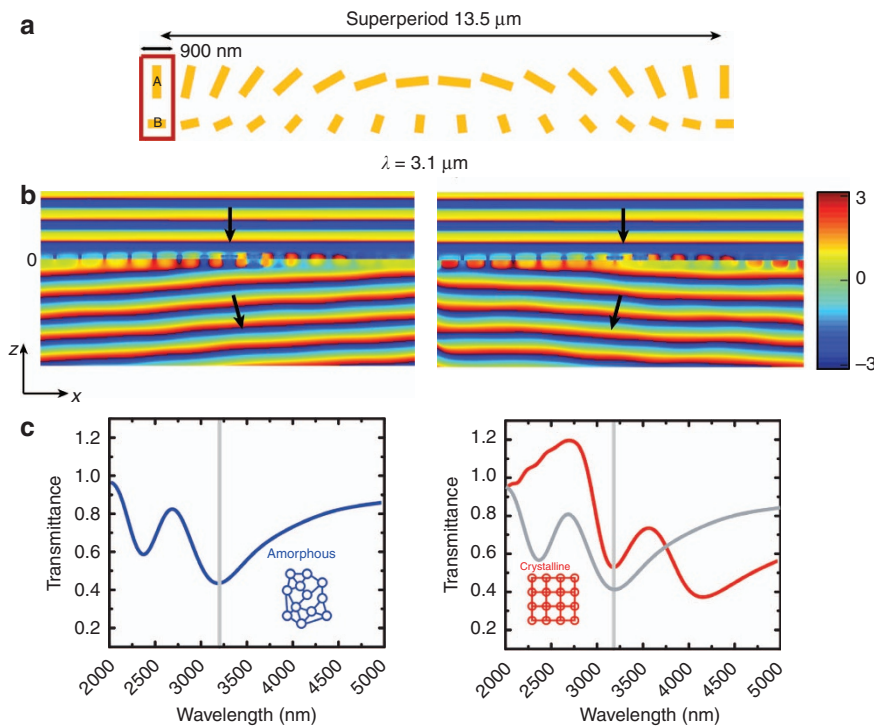


Figure 2 Working principle for active beam switching metasurface. (a) The fundamental building block consists of two rows of differently sized nano-antenna elements A and B. Antennas A are longer and resonant at $3.2\ \mu\text{m}$ for an amorphous GST substrate. The antennas are arranged such that each consecutive antenna, going from the left to the right, is clockwise rotated by 12° with respect to the previous antenna. Antennas B are shorter and resonant at $3.2\ \mu\text{m}$ for a crystalline GST substrate. They are arranged in counter-clockwise rotation. (b) Phase plots of the cross-converted scattered field (LCP) from full-field simulations with RCP light impinging. Depending on the state of the GST substrate, the beam is deviated into different directions. (c) Simulated transmittance of beam switching metasurface for a-GST and c-GST.

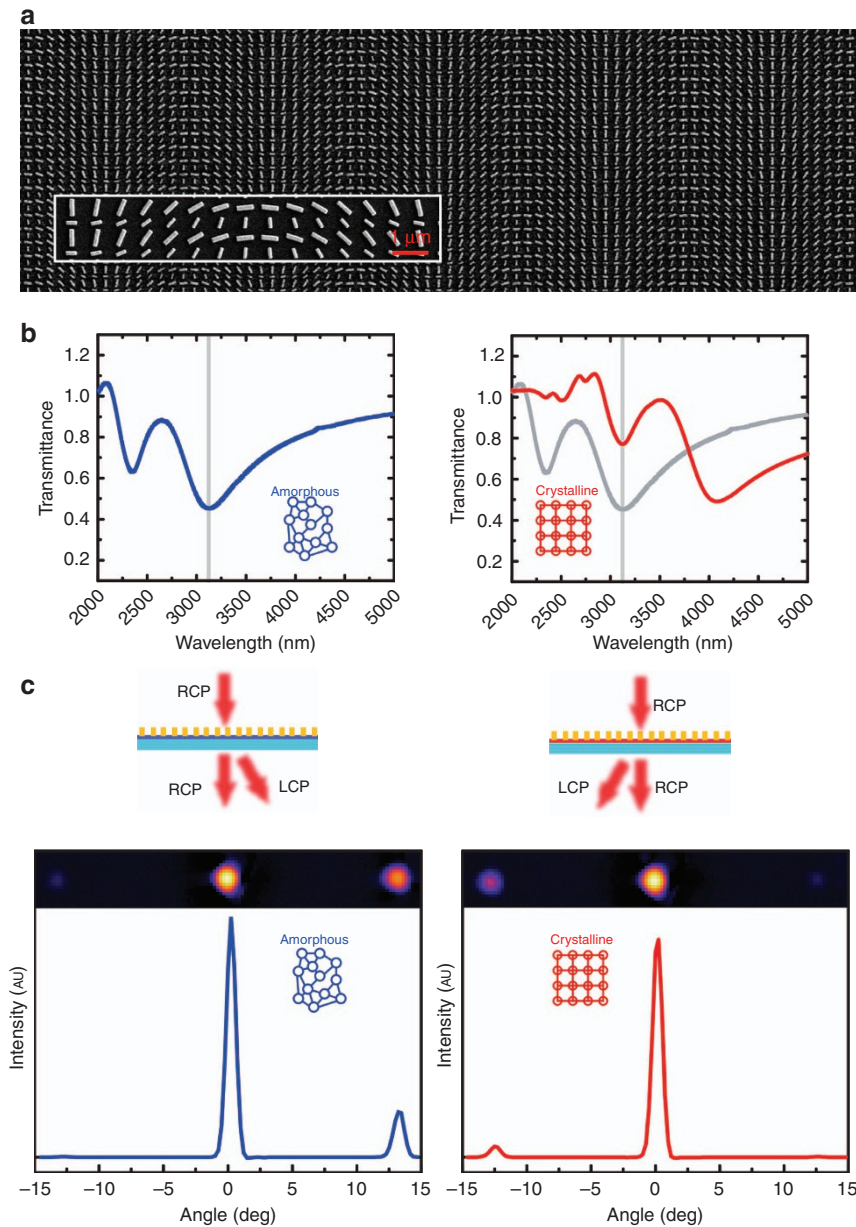


Figure 3 Experimental results of beam switching metasurface. (a) SEM micrograph of the beam switching metasurface fabricated by electron beam lithography. (b) Transmittance for the fabricated metasurface in amorphous (left) and crystalline (right) state. (c) Infrared camera images and intensity plots (same arbitrary units scale) of the beam transmitted by the active metasurface in the amorphous (left) and crystalline (right) state. As designed, the deviated beam switches to the opposite side of the main beam after inducing crystallization in the phase-change material.

order to verify the optical properties in both the amorphous and crystalline phases as well as the mechanical and chemical stability of the proposed design, we induce a single phase change in the fabricated sample. GST is amorphous as-deposited and undergoes a phase transition to the crystalline state when heated above its crystallization temperature of $T_{\text{cryst}} = 160^\circ\text{C}$. Therefore, we employ hot plate induced crystallization by heating the sample for 2 min at 180°C . Amorphization on the other hand is achieved by raising the GST temperature above its melting temperature of *ca.* $T_{\text{melt}} = 640^\circ\text{C}$ and then melt quenching it. This requires an optical or electrical pulse that selectively and rapidly only heats the GST, which subsequently dissipates its heat to the environment, in particular, the

substrate^{44,45}. Therefore, we cannot cycle the different phases using the hot plate induced heating approach.

We carried out Fourier transform infrared (FTIR) spectroscopy measurements of the same sample before and after heating using a Bruker Vertex 80 coupled to a microscope. As designed, the plasmon resonance of the longer nanorods A lies at $3.15\ \mu\text{m}$ for a-GST whereas the shorter nanorods B exhibit a resonance at $2.28\ \mu\text{m}$. In the crystalline state, the plasmon resonance associated with nanorod set B is shifted to $3.15\ \mu\text{m}$, which excellently coincides with the resonance position of antenna set A in the a-GST case. Simultaneously, the plasmon resonance of antenna set A is shifted out of the region of interest to $4.1\ \mu\text{m}$.

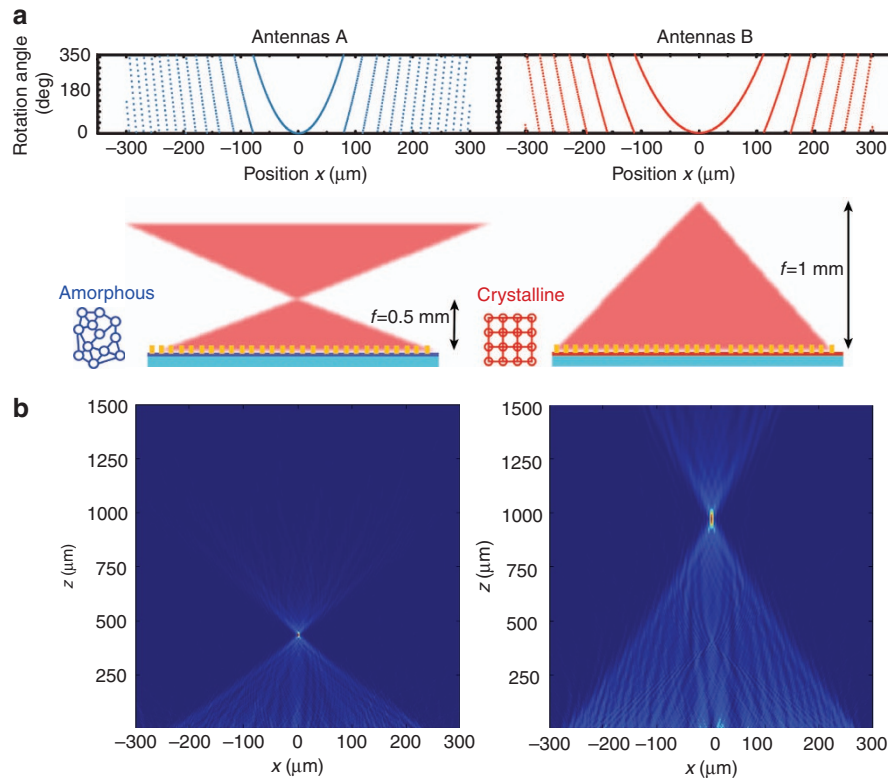


Figure 4 Working principle of cylindrical bifocal lens. As for the beam-switching metasurface, antennas A and B are line-wise alternated on a GST substrate, which yields a cylindrical lens with varying focal depending on the type of antenna, which interacts with the incident light. (a) Rotation angle versus x -position for antenna type A (left) and B (right). These distributions give rise to a focus at $z=0.5$ mm for amorphous GST and $z=1$ mm for crystalline GST. (b) Full-field simulation of field intensities arising in the amorphous (left) and crystalline (right) cases. As designed, the focus lies at $z=0.5$ mm in the amorphous case and $z=1$ mm in the crystalline case.

In both the amorphous and crystalline states, the sample was characterized as detailed in the Methods section. The resulting images for RCP illumination are shown in Figure 3c. When the GST is in its amorphous state, antenna set A interacts with the incident light and refracts the cross-converted portion of the incoming beam (LCP) to the right side of the nonconverted RCP part, which is subjected to the conventional Snell's law and therefore does not change its propagation direction. The measured deviation angle is 13.23° , in good agreement with the theoretical value of 13.28° , which can be obtained using $\alpha = \sin^{-1}(\lambda_0/A)$. For crystalline GST, the incident beam interacts with antenna set B, thus, the converted portion is refracted to the opposite direction. The relative intensity of the anomalously refracted beam in the c-GST case is lower than in the a-GST case because of the scattering of the plasmon resonance of antenna set B is weaker as can be seen in Figure 3b. This is due to the fact that the dipole strength of the shorter nanorods used for antenna set B is weaker, which is further reduced by the higher real and imaginary parts of the refractive index of c-GST. One can partially counteract this decrease in plasmon resonance amplitude by using thicker and longer nanorods for antenna set B or using two rows for each single row of antenna set A or by developing even less lossy PCMs. The measured relative efficiency, given by the intensity ratio of the anomalously refracted beam to the incident beam, is approximately 5% in accordance with previously reported values⁴⁰. Antennas A are very weakly excited (0.5% efficiency) in the c-GST case leading to the appearance of a faint side lobe at the original position.

As a second practical example, we demonstrate the concept for a bifocal cylindrical plasmonic metasurface lens. The required spatial

phase profile with the corresponding rotation angles (Figure 4a) for nanorods in antenna sets A and B are calculated over an area of $600 \mu\text{m}$ using the formula for diffractive cylindrical lenses^{10,46}

$$\varphi(x) = 0.5k_0 \left(\sqrt{f^2 + x^2} - |f| \right),$$

where φ denotes the rotation angle, f the focal length, k_0 the free space wavevector and x the associated x -position of the nanorod.

In particular, we use focal lengths $f_A=0.5$ mm for antenna set A and $f_B=1$ mm for antenna set B, that is, for amorphous GST, the focus will lie at 0.5 mm and for crystalline GST at 1 mm. The incident polarization is RCP such that the metalens will operate as converging lens¹⁰. The periodicity is kept at 900 nm in x -direction and 110 nm in y -direction with a center-to-center distance between antenna sets A and B at 550 nm.

We carried out full-field simulations over a $650 \mu\text{m}$ simulation domain with perfectly matched layers as boundaries and incident RCP plane wave illumination at $3.1 \mu\text{m}$ to verify the performance of our design (Figure 4b). The plots of the converted field intensities (LCP) reveal that indeed focusing occurs in both the amorphous and crystalline case at the chosen z -positions. We fabricated the design using the same procedure as before (see Materials and Methods section, SEM micrograph in Figure 5b) and characterized the sample at $3.1 \mu\text{m}$ wavelength with our MOPA source. Using a quarter waveplate before the active metalens, we generate RCP from the linearly polarized MOPA output and subsequently filter with an identical quarter waveplate and a linear polarizer for converted LCP light. Using a microscope with $\times 20$ magnification, we image different

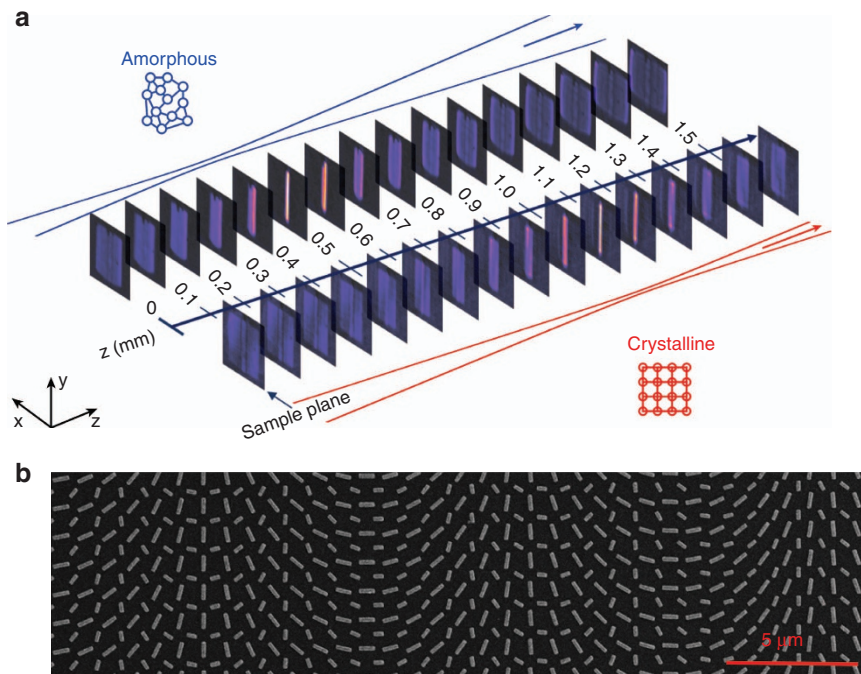


Figure 5 Experimental results for the cylindrical bifocal lens. (a) Camera pictures of the cylindrical bifocal lens imaged at different distances z from the metasurface. Since the design is for a cylindrical lens, only the x -direction is focused. In the amorphous case, a bright line appears at $z=0.5$ mm, whereas the image shows broad diffuse lightness at the same z position in the crystalline case. At $z=1$ mm the bright line focus appears in the crystalline case whereas one can only observe a light patch in the amorphous case. This is in very good agreement with the theory. (b) SEM micrograph of a portion of the fabricated cylindrical metasurface lens.

z -constant planes, revealing the beam shape at different distances from the bifocal plasmonic lens (see Supporting Information for details). The resulting images for the sample plane and $z=0.5$ and 1 mm-distances are shown in Figure 5a. When the GST is in the amorphous state, as before, only antenna set A interacts with the incoming light, thus imprinting the phase profile that creates a focus at $z=0.5$ mm, which leads to a bright line focus at this distance. After inducing a phase change to the crystalline state, as designed, antenna set B defines the functionality of the metalens. This manifests as a focal line that becomes visible at $z=1$ mm. As for the beam-switching case, antenna set A weakly interacts in the c -GST case as well leading to the appearance of a faint focal line at 0.5 mm of *ca.* 0.5% efficiency. Note, that while our demonstration used moderate numerical apertures ($NA=0.5$) in the amorphous case, it has been demonstrated that high numerical apertures of $NA=0.8$ can be achieved with a geometrical phase approach using dielectric nanofins⁴⁷. The achievable NA is only limited by how densely the spatial sampling of the phase can be carried out, which is comparable to nanofins and plasmonic antennas.

The focusing efficiency, defined as the focused intensity divided by the incoming intensity, is relatively low (*ca.* 10 % in the crystalline case and 5 % in the amorphous case) compared to high-efficiency dielectric metasurfaces. However, using plasmonic antennas as presented here has the unique benefit of being highly sensitive to the dielectric environment, which is not the case for dielectric nanofins. Hence, our design concept can only be realized in a plasmonic system.

CONCLUSIONS

In conclusion, we have presented a novel approach for designing active compact nanophotonic devices and experimentally demonstrated the feasibility in terms of optical properties, and mechanical and chemical stability at the example of a plasmonic beam switching metasurface

and a bifocal metalens. The method proposed has the benefit that it is highly integrated in a layered fashion without relying on any mechanical motion or reconfiguration. While we chose to restrict ourselves to interweaving only two functionalities per sample, it is also possible to utilize more sets of nanorods with distinct resonances. The GST layer can be partly switched from the amorphous to crystalline state (the reverse process to the amorphous state would be single-step due to it being achieved through melt quenching) to generate intermediate refractive indices that select for the different antenna sets whereby each of these states would be metastable by themselves⁴⁸. The limiting factor lies therein that more antenna sets would equal less area coverage per antenna set and therefore a weaker individual performance. However, since the functionality is only imprinted on the converted part of the beam, one can easily filter out any light that passes through the metasurface without interacting. Furthermore, a whole range of PCMs exists that all have unique optical properties³⁷ such that an additional design parameter is readily available through the choice of a particular PCM.

One is not restricted to combining similar functionalities into one active metasurface: one can easily 'mix-and-match' entirely different optical components in one active metasurface and thus create highly integrated multi-purpose nanophotonic components. Furthermore, while our demonstration relies on one-directional hot plate induced phase change, it is well-known that GST can be reversibly electrically and optically switched on ultrafast time-scales^{44,45,49}. A practical implementation of our presented design concept would ideally utilize a diced GST substrate instead of the continuous layer used in the present work. This would allow for using standard electrical switching setups known from data storage that deal with nanoscale volumes of phase-change material. For electrical switching, additionally implementing indium tin oxide cross-bar electrodes would even enable

individual addressing of GST patches. Overall, the approach presented creates an exciting new design principle that can be explored in many directions ranging from on-demand nanophotonic components, such as novel scanners combining beam switching and lensing, to dynamic phased-array optics for aberration correction and active holography.

CONFLICT OF INTEREST

The authors declare no conflict of interest.

ACKNOWLEDGEMENTS

We gratefully acknowledge financial support by the ERC Advanced Grant (COMPLEXPLAS), BMBF (13N9048 and 13N10146), the Baden Württemberg Stiftung (Internationale Spitzenforschung II), DFG (SPPI391, FOR730 and GI 269/11-1) and SFB 917 (Resistive Nanoswitches). XY and TS additionally acknowledge financial support by the Carl-Zeiss-Stiftung. We would like to thank Nikolai Strohfeldt for help with the visualization and Florian Mörz and Stefan Kedenburg for help with the optical setup. We thank DFG and University of Stuttgart for support through their open access fund.

- Sullivan LH. The tall office building artistically considered. *Lippincott's Magazine*. 1896; 403–409.
- Born M, Wolf E. *Principles of Optics* 7th edition Cambridge University Press: Cambridge, UK, 1999.
- Velzel C. *A Course in Lens Design*. Springer: The Netherlands. 2014.
- Yu NF, Genevet P, Kats MA, Aieta F, Tetienne J-P *et al*. Light propagation with phase discontinuities: generalized laws of reflection and refraction. *Science* 2011; **334**: 333–337.
- Kildishev AV, Boltasseva A, Shalaev VM. Planar photonics with metasurfaces. *Science* 2013; **339**: 1232009.
- Aieta F, Genevet P, Kats MA, Yu NF, Blanchard R *et al*. Aberration-free ultrathin flat lenses and axicons at telecom wavelengths based on plasmonic metasurfaces. *Nano Lett* 2012; **12**: 4932–4936.
- Yu NF, Capasso F. Flat optics with designer metasurfaces. *Nat Mater* 2014; **13**: 139–150.
- Yu NF, Genevet P, Aieta F, Kats MA, Blanchard R *et al*. Flat optics: controlling wavefronts with optical antenna metasurfaces. *IEEE J Sel Top Quant Electron* 2013; **19**: 4700423.
- Lu WT, Sridhar S. Flat lens without optical axis: Theory of imaging. *Opt Express* 2005; **13**: 10673–10680.
- Chen XZ, Huang LL, Mühlenbernd H, Li GX, Bai BF *et al*. Dual-polarity plasmonic metalens for visible light. *Nat Commun* 2012; **3**: 1198.
- West PR, Stewart JL, Kildishev AV, Shalaev VM, Shkunov VV *et al*. All-dielectric subwavelength metasurface focusing lens. *Opt Express* 2014; **22**: 26212–26221.
- Lin DM, Fan PY, Hasman E, Brongersma ML. Dielectric gradient metasurface optical elements. *Science* 2014; **345**: 298–302.
- Mueller JPB, Leosson K, Capasso F. Ultracompact metasurface in-line polarimeter. *Optica* 2016; **3**: 42–47.
- Pors A, Nielsen MG, Bozhevolnyi SI. Plasmonic metagratings for simultaneous determination of Stokes parameters. *Optica* 2015; **2**: 716–723.
- Papasimakis N, Luo ZQ, Shen ZX, De Angelis F, Di Fabrizio E *et al*. Graphene in a photonic metamaterial. *Opt Express* 2010; **18**: 8353–8359.
- Yao Y, Kats MA, Genevet P, Yu NF, Song Y *et al*. Broad electrical tuning of graphene-loaded plasmonic antennas. *Nano Lett* 2013; **13**: 1257–1264.
- Fang ZY, Wang YM, Schlather AE, Liu Z, Ajayan PM *et al*. Active tunable absorption enhancement with graphene nanodisk arrays. *Nano Lett* 2014; **14**: 299–304.
- Rodrigo D, Limaj O, Janner D, Etezadi D, de Abajo FJG *et al*. Mid-infrared plasmonic biosensing with graphene. *Science* 2015; **349**: 165–168.
- Chen H-T, Padilla WJ, Zide JMO, Gossard AC, Taylor AJ *et al*. Active terahertz metamaterial devices. *Nature* 2006; **444**: 597–600.
- Padilla WJ, Taylor AJ, Highstrete C, Lee M, Averitt RD. Dynamical electric and magnetic metamaterial response at terahertz frequencies. *Phys Rev Lett* 2006; **96**: 107401.
- Chen H-T, O'Hara JF, Azad AK, Taylor AJ, Averitt RD *et al*. Experimental demonstration of frequency-agile terahertz metamaterials. *Nat Photon* 2008; **2**: 295–298.
- Tao H, Strikwerda AC, Fan K, Padilla WJ, Zhang X *et al*. Reconfigurable terahertz metamaterials. *Phys Rev Lett* 2009; **103**: 147401.
- Luther JM, Jain PK, Ewers T, Alivisatos AP. Localized surface plasmon resonances arising from free carriers in doped quantum dots. *Nat Mater* 2011; **10**: 361–366.

- Dicken MJ, Aydin K, Pryce IM, Sweatlock LA, Boyd EM *et al*. Frequency tunable near-infrared metamaterials based on VO₂ phase transition. *Opt Express* 2009; **17**: 18330–18339.
- Kats MA, Blanchard R, Genevet P, Yang Z, Qazilbash MM *et al*. Thermal tuning of mid-infrared plasmonic antenna arrays using a phase change material. *Opt Lett* 2013; **38**: 368–370.
- Kats MA, Sharma D, Lin J, Genevet P, Blanchard R *et al*. Ultra-thin perfect absorber employing a tunable phase change material. *Appl Phys Lett* 2012; **101**: 221101.
- Soares BF, Jonsson F, Zheludev NI. All-optical phase-change memory in a single gallium nanoparticle. *Phys Rev Lett* 2007; **98**: 153905.
- Vivekchand SRC, Engel CJ, Lubin SM, Blaber MG, Zhou W *et al*. Liquid Plasmonics: Manipulating surface plasmon polaritons via phase transitions. *Nano Lett* 2012; **12**: 4324–4328.
- Strohfeldt N, Tittl A, Schäferling M, Neubrech F, Kreibig U *et al*. Yttrium hydride nanoantennas for active plasmonics. *Nano Lett* 2014; **14**: 1140–1147.
- Sterl F, Strohfeldt N, Walter R, Griessen R, Tittl A *et al*. Magnesium as novel material for active plasmonics in the visible wavelength range. *Nano Lett* 2015; **15**: 7949–7955.
- Gholipour B, Zhang JF, MacDonald KF, Hewak DW, Zheludev NI. An all-optical, non-volatile, bidirectional, phase-change meta-switch. *Adv Mater* 2013; **25**: 3050–3054.
- Michel A-KU, Chigrin DN, Maß TWW, Schönauer K, Salinga M *et al*. Using low-loss phase-change materials for mid-infrared antenna resonance tuning. *Nano Lett* 2013; **13**: 3470–3475.
- Tittl A, Michel A-KU, Schäferling M, Yin XH, Gholipour B *et al*. A switchable mid-infrared plasmonic perfect absorber with multispectral thermal imaging capability. *Adv Mater* 2015; **27**: 4597–4603.
- Yin XH, Schäferling M, Michel A-KU, Tittl A, Wuttig M *et al*. Active chiral plasmonics. *Nano Lett* 2015; **15**: 4255–4260.
- Wang Q, Rogers ETF, Gholipour B, Wang C-M, Yuan GH *et al*. Optically reconfigurable metasurfaces and photonic devices based on phase change materials. *Nat Photon* 2016; **10**: 60–65.
- Mörz F, Steinle T, Steinmann A, Giessen H. Multi-Watt femtosecond optical parametric master oscillator power amplifier at 43 MHz. *Opt Express* 2015; **23**: 23960–23967.
- Shportko K, Kremers S, Woda M, Lencer D, Robertson J *et al*. Resonant bonding in crystalline phase-change materials. *Nat Mater* 2008; **7**: 653–658.
- Glybovski SB, Tretyakov SA, Belov PA, Kivshar YS, Simovski CR. Metasurfaces: From microwaves to visible. *Phys Rep* 2016; **634**: 1–72.
- Munk BA. *Frequency Selective Surfaces: Theory and Design*. John Wiley & Sons: Hoboken, NJ, USA. 2005.
- Huang LL, Chen XZ, Mühlenbernd H, Li GX, Bai BF *et al*. Dispersionless phase discontinuities for controlling light propagation. *Nano Lett* 2012; **12**: 5750–5755.
- Chen WT, Yang K-Y, Wang C-M, Huang Y-W, Sun G *et al*. High-efficiency broadband meta-hologram with polarization-controlled dual images. *Nano Lett* 2014; **14**: 225–230.
- Arbabi A, Horie Y, Bagheri M, Faraon A. Dielectric metasurfaces for complete control of phase and polarization with subwavelength spatial resolution and high transmission. *Nat Nanotechnol* 2015; **10**: 937–943.
- Ellenbogen T, Seo K, Crozier KB. Chromatic plasmonic polarizers for active visible color filtering and polarimetry. *Nano Lett* 2012; **12**: 1026–1031.
- Bruns G, Merkelbach P, Schlockermann C, Salinga M, Wuttig M *et al*. Nanosecond switching in GeTe phase change memory cells. *Appl Phys Lett* 2009; **95**: 043108.
- Michel A-KU, Zalden P, Chigrin DN, Wuttig M, Lindenberg AM *et al*. Reversible optical switching of infrared antenna resonances with ultrathin phase-change layers using femtosecond laser pulses. *ACS Photon* 2014; **1**: 833–839.
- Hirayama K, Glytsis EN, Gaylord TK, Wilson DW. Rigorous electromagnetic analysis of diffractive cylindrical lenses. *J Opt Soc Am A* 1996; **13**: 2219–2231.
- Khorasaninejad M, Chen WT, Devlin RC, Oh J, Zhu AY *et al*. Metalenses at visible wavelengths: Diffraction-limited focusing and subwavelength resolution imaging. *Science* 2016; **352**: 1190–1194.
- Chen YG, Kao TS, Ng B, Li X, Luo XG *et al*. Hybrid phase-change plasmonic crystals for active tuning of lattice resonances. *Opt Express* 2013; **21**: 13691–13698.
- Hosseini P, Wright CD, Bhaskaran H. An optoelectronic framework enabled by low-dimensional phase-change films. *Nature* 2014; **511**: 206–211.



This work is licensed under a Creative Commons Attribution-NonCommercial-NoDerivs 4.0 International License. The images or other third party material in this article are included in the article's Creative Commons license, unless indicated otherwise in the credit line; if the material is not included under the Creative Commons license, users will need to obtain permission from the license holder to reproduce the material. To view a copy of this license, visit <http://creativecommons.org/licenses/by-nc-nd/4.0/>

© The Author(s) 2017

Supplementary Information for this article can be found on the *Light: Science & Applications*' website (<http://www.nature.com/lisa>).